

1
2
3
4 *Are microstructures in plutonic rocks primary or secondary?: a re-*
5 *examination of the metasomatism hypothesis for the roof-sourced autoliths*
6 *in the Skaergaard intrusion.*
7
8

9 Marian B. Holness¹, Jens C. Ø. Andersen², Olivier Namur³, and Troels F.D. Nielsen⁴
10

11 1. Department of Earth Sciences, University of Cambridge, Downing Street, Cambridge CB2 3EQ,
12 UK. Email: marian@esc.cam.ac.uk

13 2. Camborne School of Mines, University of Exeter, Penryn Campus, Tremough, Penryn TR10 9FE,
14 UK

15 3. Department of Earth and Environmental Sciences, KU Leuven, Celestijnlaan 200E, 3001 Leuven,
16 Belgium

17 4. Department for Mapping and Mineral Resources, Geological Survey of Denmark and Greenland,
18 Øster Voldgade 10, 1350 Copenhagen K, Denmark
19

20 November 2023
21

22 **Abstract**

23 The roof-derived autoliths in the floor cumulates of the Skaergaard Intrusion have been argued to have
24 been extensively metasomatized and recrystallised, forming the foundation of the hypothesis that
25 microstructures in plutonic rocks are essentially metamorphic. However, the augite-plagioclase-
26 plagioclase dihedral angles and plagioclase core composition of the autoliths match with those of the
27 roof rocks, demonstrating that they were generally solid on arrival at the floor, with no subsequent
28 microstructural or compositional modification. Many autoliths have mafic rinds, which were used as
29 evidence of metasomatism: these rinds fall into two groups. The rarely developed rind rock of Irvine
30 *et al.* (1998) is most likely chilled magma infiltrating along fractures in the roof rocks, either associated
31 directly with detachment of roof material, or occurring before final detachment. Thin mafic rims are
32 widespread in LZc and MZ, present at the tops of the more elongate autoliths, with a corresponding
33 felsic rim at the base of the most elongate. The close correspondence of thin rim development with
34 autolith shape, rather than composition, is argued to be evidence that they formed as a result of
35 differential migration of immiscible conjugate interstitial liquids: the dense Fe-rich liquid flowed
36 downwards and ponded on the tops of impermeable autoliths, whereas its buoyant Si-rich conjugate
37 flowed upwards and was trapped underneath. Any differences in microstructure and bulk composition
38 of the autoliths compared to the remaining exposures of the roof sequence reflect the wider range of
39 lithologies in the now-eroded regions of the roof.
40

41 INTRODUCTION

42 A number of studies have argued that the microstructures, and even compositions, of layered mafic
43 intrusions are not primary, but have been significantly modified during cooling (e.g. McBirney & Hunter,
44 1995; McBirney 2009; Boudreau, 2011; Bartley *et al.* 2018; Glazner *et al.*, 2020). A particular example
45 used to support and develop this hypothesis is that of the abundant autoliths in the floor cumulates of
46 the Skaergaard Intrusion of East Greenland, which, following Wager & Brown (1968), are universally
47 agreed to have fallen from the inwards-solidifying intrusion roof. It has been argued that their mafic
48 components have been extracted (by some unspecified process) to form melanocratic rinds around a
49 relatively anorthositic centre, and that modal layering and foliation were imposed once they reached
50 the intrusion floor (McBirney, 1979; 1987; 1995; 2009; McBirney & Sonnenthal, 1990; McBirney &
51 Hunter, 1995), though Irvine (1987) and Irvine *et al.* (1998) argued against this interpretation.

52 Here we present the results of a detailed microstructural investigation of both autoliths and the
53 remaining exposures of the intrusion roof, together with a consideration of plagioclase composition
54 and larger-scale field observations. We also examine the melanocratic rinds, distinguishing between
55 those described by Irvine *et al.* (1998) and attributed to the chilling of magma infiltrating along fractures
56 in the roof sequence, and the localised development of Fe-Ti oxide-rich rinds. Our results support the
57 contention of Irvine *et al.* (1998) that the cognate xenoliths were almost invariably entirely solid when
58 detached from the roof and that no microstructural or compositional changes occurred after they
59 arrived at the intrusion floor. We argue that the Fe-Ti oxide-rich rinds are bodies of an unmixed Fe-
60 rich interstitial liquid that ponded on the tops of the impermeable autoliths. Instead of forming part of
61 the foundation of the hypothesis that plutonic microstructures are generally extensively overprinted,
62 both the compositions and microstructures in these autoliths are primary.

63

64 GEOLOGICAL SETTING

65 The Palaeogene (56.02 Ma: Wotzlaw *et al.*, 2012) Skaergaard Intrusion, East Greenland (Figure 1),
66 is associated with the opening of the North Atlantic Ocean. It comprises an 8 km x 11 km x 4 km body
67 (Nielsen, 2004) of tholeiitic magma rapidly emplaced (Annen *et al.*, 2022) in a fault-bounded opening
68 at the unconformity between basement Archean gneisses and overlying Cretaceous-Palaeocene
69 sediments and Paleogene flood basalts (Wager & Deer, 1939; McBirney, 1989a). It fractionated as a
70 closed system once the chamber was filled. The intrusion is now tilted towards the south-east by ~20°,
71 resulting in an almost complete section through the stratigraphy of the floor cumulates, accompanied
72 by the loss of most of the intrusion roof (Wager & Brown, 1968).

73 The intrusion is divided into three main units: the Layered Series, Marginal Border Series (MBS) and
74 Upper Border Series (UBS), which crystallized inwards from the floor, walls, and roof respectively and
75 display correlated changes in liquidus assemblage. The Layered Series is subdivided into Lower,
76 Middle and Upper Zones (LZ, MZ, and UZ, respectively), based on the absence of cumulus olivine in

77 the Middle Zone. The Lower Zone is further subdivided: LZa contains cumulus olivine and plagioclase;
78 the base of LZb is marked by the arrival of cumulus augite; and the base of LZc is marked by the
79 arrival of cumulus Fe-Ti oxides. Upper Zone is also subdivided; the base of UZb defines the arrival of
80 cumulus apatite, while the base of UZc marks the first appearance of the mosaic form of ferro-
81 hedenbergite inverted from β -ferrobustamite. The Layered Series is underlain by a quantity of
82 unexposed floor cumulates termed the Hidden Zone (HZ) by Wager & Deer (1939), thought to be of
83 the order of 150 m thick in the region of the Uttental Plateau, and with the same primocryst assemblage
84 as LZa (Maaløe, 1976; Holness *et al.*, 2007a; b; 2015).

85

86 **The Upper Border Series**

87 All remaining UBS exposures are at the extreme south of the intrusion (Figures 1, 2): the UBS is
88 thought to have originally comprised $\sim 1/6$ of the total volume of the intrusion, with an average thickness
89 of ~ 600 m (Nielsen, 2004). Its lower part has been intruded by the mafic Basistoppen sill, together
90 with several minor granophyric sills (Figure 2). It was subdivided by Wager (1960) into Upper Border
91 Group α , β and γ , with a hypothetical outermost portion assigned to Upper Border Group ultra- α (Figure
92 2), correlated with the Layered Series on the basis of plagioclase core composition (Wager & Brown,
93 1968; Figure 2). The first three subdivisions are equivalent to the Layered Series LZ, MZ and UZ,
94 respectively, with ultra- α equivalent to HZ. The UBS contains much less olivine than the equivalent
95 parts of the Layered Series, attributed by Wager & Deer (1939) to gravitationally driven loss of dense
96 mafic grains, and by Wager & Brown (1968) to contamination by the felsic gneiss country rock. Apart
97 from the fine-grained outermost regions, the UBS is commonly coarser-grained than the Layered
98 Series: a similar relatively coarse grain size of the MBS was attributed by Holness *et al.* (2022) to a
99 predominance of *in situ* nucleation and this is likely also to apply to the UBS.

100 Because the UBS is richer overall in SiO_2 , K_2O , P_2O_5 and incompatible trace elements compared to
101 the Layered Series, Naslund (1984a) argued that it crystallised from a separate body of magma with
102 a relatively early appearance of apatite primocrysts. He subdivided the UBS into an outer Upper Border
103 Zone τ , followed by Upper Border Zones α (plagioclase, olivine and apatite primocrysts), β (plagioclase
104 and Ca-rich pyroxene) and γ (all four minerals: Figure 2). However, re-examination by Salmonsens &
105 Tegner (2013) confirmed the Wager (1960) subdivisions, now denoted LZ', MZ' and UZ': they differ
106 from Wager (1960) in placing the boundary between LZ' and MZ' (Wager's α and β) at An_{50} , instead
107 of An_{53} , with the Sandwich Horizon at An_{21} instead of An_{34} (though it should be noted that there is a
108 variability of ~ 5 mol.% at any one stratigraphic level: Namur & Humphreys, 2018). They place the
109 boundary between LZa' and LZb' at An_{59-60} , that between LZb' and LZc' at An_{52} , and that between
110 LZc' and MZ' at An_{50} . The base of UZ' is placed at An_{44} , with the two boundaries between the
111 subdivisions in UZ' at An_{40} (apatite-in) and $\text{An}_{32\pm 2}$ (ferrobustamite-in). In this contribution, we use the
112 subdivision scheme of Salmonsens & Tegner (2013) (Figure 2).

113 The inaccessibility of much of the terrain prevents detailed mapping of the UBS. However, the current
114 exposure contains a clearly-defined major unconformity, with much of MZ' missing in the region of
115 Brødretoppen (Wager & Brown, 1968; Figure 2). The complete UBS stratigraphy is only exposed on
116 the eastern side (Salmonsén & Tegner, 2013; Figure 2).

117

118 **Liquid immiscibility in the Skaergaard Intrusion**

119 The Skaergaard mass-balanced liquid line of descent encountered the silicate liquid binode during
120 fractionation, splitting into Fe-rich and Si-rich conjugates (McBirney & Nakamura, 1974; McBirney,
121 1975), at a composition equivalent to the bulk melt near the base of UZb (Nielsen *et al.*, 2019). This
122 is recorded by coexisting Si- and Fe-rich melt inclusions in primocryst apatite from UZb (Jakobsen *et al.*,
123 2005), and the co-existence in the upper part of the Layered Series of grain-scale bodies of
124 interstitial granophyre (formed from the solidification of the Si-rich conjugate) and interstitial
125 intergrowths dominated by ilmenite, magnetite and clinopyroxene which represent the solidified Fe-
126 rich conjugate (Holness *et al.*, 2011; Humphreys, 2011). On the grain scale, granophyric pockets are
127 confined to plagioclase-rich regions whereas the ilmenite-rich pockets are surrounded by olivine and
128 pyroxene (Holness *et al.*, 2011), consistent with the different wetting properties of the immiscible
129 conjugates (Honour *et al.*, 2019).

130 The Si-rich liquid is buoyant and viscous whereas its Fe-rich conjugate is dense and relatively inviscid
131 (Namur *et al.*, 2015), creating the potential for differential migration. The systematic loss of an exsolved
132 buoyant Si-rich liquid from the fractionating interstitial liquid in the mush on the chamber floor, and its
133 addition to the overlying bulk magma, is argued to have resulted in an overall Fe-enrichment of the
134 Layered Series from LZc upwards, with a corresponding Si-enrichment in UBS (Nielsen *et al.*, 2019).
135 Outcrop-scale evidence of differential migration of unmixed immiscible conjugates in the mush is
136 provided by paired, irregularly shaped, felsic and mafic bodies of late-stage segregated liquid (Figure
137 3; McBirney, 1975; Sonnenthal, 1992; Larsen & Brooks, 1994). In all cases, the mafic component
138 (comprising olivine pyroxenite, with variable amounts of Fe-Ti oxides) occurs beneath the associated
139 felsic material, either forming the lower part of a single segregation or a separate body. The paired
140 felsic and mafic bodies are closely spatially associated with coarse-grained pegmatitic segregations
141 that occur through much of the Layered Series (Wager & Deer, 1939; Wager & Brown, 1968; McBirney
142 & Noyes, 1979; McBirney & Sonnenthal, 1990; Larsen & Brooks, 1994). These pegmatites are
143 rounded and diapir-like in the lower parts of the Layered Series, but comprise layer-parallel sills and
144 sharply defined dykes above the upper parts of MZ, attributable to a reduction in the porosity of the
145 mush (Larsen & Brooks, 1994), and consistent with a reduction in mush thickness from ~100m in LZ
146 to a few metres at the UZa/b boundary (Holness *et al.*, 2017a).

147 Grain-scale evidence of pervasive differential migration of the immiscible liquids in the mush is
148 provided by the presence of two fractionation trends in intercumulus plagioclase (Humphreys, 2011),
149 attesting to a breakdown of chemical communication between the two immiscible conjugates. It is also

150 manifest in LZc and MZ by the development of reactive symplectites formed of anorthitic plagioclase
151 and olivine (or pyroxene) rooted on Fe-Ti oxide grains and replacing the surrounding primocrysts of
152 plagioclase and (less commonly) olivine and augite (the Type I symplectites of Holness *et al.*, 2011).
153 In LZc and MZ, Type I symplectites are accompanied by olivine rims separating Fe-Ti oxides from
154 plagioclase and augite primocrysts (Figure 4a; Wager & Deer, 1939; Nwe, 1976; Nielsen *et al.*, 2015).
155 They are monocrystalline in rocks containing olivine primocrysts (primarily in LZc), with the rims
156 extending from nearby grains in which they are in optical continuity. Where primocryst olivine is absent
157 (i.e. MZ) the rims are polycrystalline (Holness *et al.*, 2011). The oxide-rich gabbros in LZc and MZ,
158 containing highly irregular and extensive aggregates of Fe-Ti oxides, are notable for the
159 recrystallisation of clinopyroxene primocrysts to form a mosaic of small grains (Figure 4): this
160 combination of reactive symplectites, abundant anhedral oxides, olivine rims and recrystallised
161 pyroxene, known as Paragenesis 2, is argued to result from the crystallisation of ponded Fe-rich
162 interstitial liquid out of chemical equilibrium with the earlier-formed liquidus paragenesis (Nielsen *et al.*,
163 2015).

164

165 **ROOF-DERIVED AUTOLITHS IN THE LAYERED SERIES**

166 The MBS and the lowest exposed parts of the Layered Series contain xenoliths of both gneissic (Markl,
167 2005; Figure 5a) and basaltic country rock, together with picritic xenoliths (Figure 5b) thought to be
168 sourced from a nearby wehrlite plug (Kays & McBirney, 1982). Some xenoliths from the overlying
169 plateau basalts forming the roof of the intrusion (Figure 5c) are present in MZ near the south of
170 Kraemer Ø (Irvine *et al.*, 1998), but the predominant type of blocks in the Layered Series is material
171 derived from the UBS (Figure 5d).

172 The roof-derived autoliths occur from the top of LZa to the middle of UZb, and are particularly abundant
173 in LZb, LZc and the lower half of MZ (Figure 1). They concentrate in stratigraphic zones 50–100 m
174 thick, extending laterally up to 1 km, and range in size from a few 10's of cm up to several hundreds
175 of metres (Irvine *et al.*, 1998). They commonly appear leucocratic relative to the surrounding gabbroic
176 cumulates (Figure 5d), with a variable shape, though most are slab-like and oriented parallel to the
177 layering in the host gabbro, with sharply-defined margins on the grain-scale (Figure 6a). Irvine *et al.*
178 (1998) describe an autolith in UZa with a cleanly broken upper surface, but an irregular lower margin,
179 suggestive of incomplete solidification on arrival at the floor. The grain-size in the autoliths is generally
180 different to that of their host, being commonly coarser-grained.

181 Following Wager & Brown (1968; p.136), who argued that many of the autoliths found in MZ on
182 Kraemer Ø are derived from LZ', Irvine *et al.* (1998) divided the autoliths into three types: gabbroic
183 troctolite; gabbroic anorthosite; and oxide gabbro. Gabbroic troctolite (scans of thin sections of typical
184 examples are provided in the Supplementary Appendix) is a plagioclase cumulate with minor amounts
185 of olivine (which may be poikilitic) and interstitial augite: autoliths of this lithology appear in LZa and
186 are found at all levels up to UZb. On the basis of plagioclase composition, Irvine *et al.* (1998) assign

187 this lithology to the UBS equivalent of HZ, with some overlap with the LZa equivalent. Gabbroic
188 anorthosite is relatively uncommon and is dominated by plagioclase primocrysts with sub-poikilitic
189 augite: olivine is absent (scans provided in the Supplementary Appendix). Gabbroic anorthosite
190 autoliths are found in LZb and MZ: Irvine *et al.* (1998) assign this lithology to the UBS equivalent of
191 LZb. Oxide gabbro is generally coarse-grained relative both to the other autolith types and to the
192 gabbros of the Layered Series, and contains primocrysts of plagioclase, augite, and Fe-Ti oxide (scans
193 provided in the Supplementary Appendix). Small amounts of olivine may be present. Oxide gabbro
194 autoliths are found only in the lower two-thirds of MZ, and are assigned by Irvine *et al.* (1998) to the
195 UBS equivalent of LZc, although the plagioclase composition also overlaps with that of MZ* (in the
196 MBS).

197 Irvine *et al.* (1998) report weak concentrations of Fe-Ti oxides, only 1–2 mm thick, along the top
198 surfaces of many small autoliths in MZ (an example is shown in their Figure 24D). They also report
199 that a small number of the medium-sized to large autoliths of all three different compositional
200 categories are bordered by pale brown weathering, fine-grained, mafic to ultramafic rinds 5–15 cm
201 thick, known as rind rock, dominated by augite, plagioclase and Fe-Ti oxides, with rare olivine (Figure
202 7). Rind rock has a well-defined and sharp contact against the autolith, but a gradational contact with
203 the gabbroic host: grainsize increases from the autolith contact into the gabbroic host. Rind rock also
204 forms small dykes in some of the larger autoliths, some of which have a coarser-grained central part:
205 the dykes are truncated at the autolith edges. The main occurrences of this relatively rare phenomenon
206 are in LZc and the lower half of MZ on Kraemer Ø: no rinds were recognized on stratigraphically higher
207 autoliths. Irvine *et al.* (1998) suggest rind rock represents injections of magma into fractures that
208 developed during disintegration of the UBS, with the large size of the autoliths on which they are found
209 contributing to a rapid chilling and consequent fine grainsize. They further suggest there might have
210 been some reaction between the injecting magma and the autolith.

211

212 **THE HYPOTHESIS OF METASOMATIC REPLACEMENT OF THE AUTOLITHS**

213 The first suggestion that autoliths found in the Layered Series had undergone metasomatic
214 replacement following their arrival at the floor was made by McBirney (1979). He argued that a
215 magnetite-rich layer surrounding a basaltic xenolith in MZ (Figure 5c) was formed by the removal of
216 mafic components from the autolith, together with migration of mafic material from the surrounding
217 gabbro. He suggested this metasomatism was a consequence of a difference in the oxidation states
218 between the autolith and the liquid on the floor. No mechanism was proposed, and the only detailed
219 work demonstrating changes in bulk composition or mineralogy was reported by Irvine (1979), who
220 found evidence of only limited interaction with the adjoining cumulates.

221 The concept of metasomatic alteration was expanded by McBirney (1987) to include the roof-derived
222 autoliths, based on the assumption that their relatively felsic nature would have prevented them sinking
223 to the floor (Naslund, 1986), together with their more anorthitic plagioclase, and lower bulk Fe, Ti, K

224 and P contents compared their putative source in the UBS. It was argued that metasomatism was
225 accompanied by wholesale recrystallisation resulting in propagation of layering present in the
226 surrounding gabbros into the autoliths. McBirney (1989a) further developed the metasomatic
227 hypothesis by suggesting that the mafic components removed from the autoliths form iron-rich
228 selvages and paired bodies of anorthosite and mafic material (e.g. Figure 3), in a similar manner to
229 his suggestion for the basaltic xenolith (McBirney, 1979). No detailed arguments were provided for
230 this process, and it is not clear whether the iron-rich selvages are equivalent to the Irvine *et al.* (1998)
231 rind rock.

232 These ideas were expanded by McBirney & Hunter (1995), who argued that microstructures in layered
233 intrusions are essentially metamorphic, with wholesale recrystallisation caused by “an anisotropy in
234 the environment in which the crystals grew”. McBirney (2009) strengthened his earlier statements
235 about the felsic nature of the autoliths by saying that metasomatism resulted in them becoming almost
236 pure anorthosite, with the mechanism for this extreme version of the metasomatic hypothesis argued
237 to be re-melting of extensively hydrothermally altered autoliths once they arrived at the floor, with their
238 mafic components carried into the surrounding gabbro by volatile-rich liquid. A quantitative model of
239 the metasomatic process was presented by Sonnenthal & McBirney (1998), involving diffusion in a
240 melt phase.

241 Dissent was expressed by Irvine (1987), who pointed out that not only does layering *not* propagate
242 into the autoliths from the surrounding gabbros, but there is no evidence of any intermediate stages
243 of metasomatic replacement. Autoliths have sharply defined margins (e.g. Figure 6a), and some
244 contain well-defined internal boundaries between units of different composition that are at a different
245 orientation to the layering in the host gabbros. The autoliths generally have plagioclase core
246 compositions different from that of the cumulus plagioclase of their host (Irvine *et al.*, 1998).
247 Furthermore, differences of $\delta^{18}\text{O}$ between the autoliths and their host (Taylor & Forrester, 1979)
248 precludes metasomatism after they left their source at the roof. The only exceptions to this are some
249 of the very smallest autoliths, which develop a centimetric-scale diffuse feldspathic margin: Irvine *et al.*
250 *al.* (1998) suggest this very localised replacement was perhaps facilitated by volatile-rich fluids.

251

252 **CHOICE OF SAMPLES AND ANALYTICAL METHODS**

253 **Samples**

254 We examined a suite of samples collected from the UBS by Lawrence Wager and Alex Deer during
255 the 1935-6 expedition, with further UBS samples from the Exchange Collection collected by Alex Deer
256 in 1966 (locations are shown in Figure 2), all housed in the Harker Collection of the Sedgwick Museum,
257 University of Cambridge. We examined autoliths from Uttental Plateau and Kraemer Ø (locations
258 shown in Figure 1). We also examined the autolith in UZa on the Skaergaard Peninsula interpreted by
259 Irvine *et al.* (1998: p. 1414) as having been only partially solidified on arrival at the floor (samples

260 SK11-B9-9 and -10). Most autoliths were sampled in their centres, but a small sub-set were also
261 sampled at their margin. Samples were also taken of the host gabbro within a few metres of some
262 autoliths. Examples of rind rock were collected from the autoliths illustrated by Irvine *et al.* (1998) in
263 their Figures 17a, 21b, 22 and 23.

264

265 **The geometry of three-grain junctions**

266 In most gabbros and dolerites, the geometry of three-grain junctions involving two grains of plagioclase
267 and one of augite, parameterised by the median value of the clinopyroxene-plagioclase-plagioclase
268 dihedral angle population, Θ_{cpp} , is lower than the equilibrium value of $109^\circ \pm 2^\circ$, due to a cooling rate
269 control on the relative rates of growth of the two minerals during solidification (Holness *et al.*, 2012a;
270 Fowler & Holness, 2022). In layered intrusions, Θ_{cpp} changes in a step-wise manner due to changes
271 in the contribution of the latent heat of crystallisation to the overall enthalpy budget on the arrival of a
272 new liquidus phase (Morse, 2011; Holness *et al.*, 2013; Holness, 2015). In the Skaergaard intrusion,
273 there is a step-wise increase in Θ_{cpp} corresponding to the arrival of liquidus augite (the LZa/b
274 boundary), another at the arrival of liquidus Fe-Ti oxides (the LZb/c boundary) and a third
275 corresponding to the arrival of liquidus apatite (the UZa/b boundary).

276 True, 3D, clinopyroxene–plagioclase–plagioclase dihedral angles were measured using a four-axis
277 Leitz universal stage mounted on a James Swift monocular microscope, with a UM32 Leitz long
278 working distance objective and a x10 eyepiece. The median value of a population of angles can be
279 determined satisfactorily with only 25 measurements (Riegger & van Vlack, 1960), although reduction
280 of the 95% confidence intervals about the median to less than $\pm 3\text{-}4^\circ$ [calculated according to the
281 method of Stickels & Hücke (1964)] generally requires more than 25 (Holness, 2010). We report the
282 median values of populations of 25 - 70 individual measurements of true 3D dihedral angles in each
283 sample.

284

285 **Plagioclase compositions**

286 The major element composition (Na, Si, Al, K, Ca and Fe) of plagioclase was determined using either
287 a Cameca SX100 electron microprobe at the Department of Earth Sciences, University of Cambridge,
288 or a JEOL JXA-8600 Superprobe at the Geologisk Institut, Aarhus University. Analysis at both
289 Cambridge and Aarhus used a defocused (5 μm) beam, with accelerating voltage of 15 keV and a
290 10nA beam current. Peak count times were 60 s for Fe and 10 s for all other elements, with the total
291 background count times equivalent to the on-peak time for each element. Primary calibrations were
292 undertaken using appropriate mineral standards and measurements were internally calibrated using
293 a Smithsonian Microbeam Standard (Labradorite 115900) to ensure consistency across multiple
294 analytical sessions. Totals <98 wt.% and >101 wt.% were discarded. Analytical uncertainties were
295 estimated through repeat analysis of Smithsonian standards, with major (>5wt%) and minor (>0.5
296 wt.%) element 1σ precisions better than 0.6 wt.% and 0.1 wt.% respectively. The average composition

297 of plagioclase was determined in Cambridge by measuring 3 spots in the centres of 6 – 9 grains:
298 analyses that were significantly more albitic than the rest of the data points were discarded on the
299 assumption that an evolved outer rim had inadvertently been analysed. Plagioclase core compositions
300 were determined in Aarhus from 2-5 grains in each thin section.

301

302 **NEW OBSERVATIONS**

303 **Microstructures in the UBS**

304 The outermost parts of the UBS (HZ' and LZa': scans of representative thin sections are provided in
305 the Supplementary Appendix) contain abundant, randomly oriented, tabular plagioclase primocrysts
306 with large, unzoned cores. In common with much of the rest of UBS, plagioclase is randomly oriented,
307 with irregular grain boundaries indicative of *in situ* growth to impingement (Figure 8a): isolated strongly
308 laminated horizons occur in LZ', defined by thin (0.3 mm) plagioclase plates up to 1 cm across (Plate
309 22 of Wager & Deer, 1939). Olivine commonly forms small subhedral grains but may also be ophitic
310 (Figure 8b). Variable amounts of interstitial augite are present, with an inwards increase in mode. In
311 HZ' and LZa', augite is commonly poikilitic (Figure 8b), and the median value of the clinopyroxene-
312 plagioclase-plagioclase dihedral angle, Θ_{cpp} , is 84.5 – 86° (data are summarised in Table 1, with full
313 data-set in the Supplementary Appendix). A sample of LZa equivalent from the topmost part of the
314 MBS on the east margin of the intrusion (at Udløberen, Figure 2) also has the same value of Θ_{cpp}
315 (Table 1).

316 The change from interstitial to primocryst clinopyroxene (the LZa'/LZb' boundary) is marked by a
317 reduction in the number of plagioclase inclusions, a progression to a subhedral or ophitic habit (scans
318 of representative thin sections are provided in the Supplementary Appendix), and the appearance of
319 simple twins parallel to the long axis, indicative of a primocrystic origin (Holness *et al.*, 2022). This is
320 associated with a step-wise increase in the median value of Θ_{cpp} to 89.5 – 91°: this is also observed
321 in a sample of LZb equivalent from the topmost part of the MBS on the east margin of the intrusion (at
322 Udløberen, Figure 2, Table 1, Supplementary Appendix).

323 Fe-Ti oxides are anhedral through much of the UBS, commonly with a skeletal or dendritic habit (scans
324 of thin sections provided in the Supplementary Appendix). The LZb'/LZc' boundary is marked by an
325 increase in oxide mode, with abundant small euhedral grains of both magnetite and ilmenite (Figure
326 8e). This is associated with a decrease in grain size, increase of clustering, and a less compact habit
327 of the augite, and a second step-wise increase in Θ_{cpp} to 94 – 94.5°.

328 In the more evolved parts of the UBS, augite reverts to being highly anhedral (Figure 8c), with some
329 dendritic grains (Figure 8d). Dihedral angles were not measured in UZ', as the abundance of
330 granophyre and the highly anhedral augite habit means there are no suitable three-grain junctions.
331 Euhedral grains of apatite are present, and locally abundant, throughout UBS (Naslund, 1984a),

332 particularly in pockets of granophyre, though in the more evolved parts it commonly has a hopper or
333 skeletal habit. The boundary between UZa' and UZb' is marked by an increase in apatite mode and
334 the appearance of apatite inclusions in primocrysts of augite and plagioclase. The lowermost horizons
335 of the UBS contain polycrystalline aggregates of hedenbergite, interpreted as inverted β -
336 ferrobustamite, consistent with them belonging to UZc (Salmonsén & Tegner, 2013)'.

337 Although the Paragenesis 2 olivine rims separating Fe-Ti oxides from plagioclase and augite
338 primocrysts that are a prominent feature of MZ (Figure 4a) are present in the equivalent subdivision
339 of the MBS (Holness *et al.*, 2022), they are absent in UBS. Type I symplectites (Figure 4a) are rare
340 and confined to the outermost parts of the UBS.

341 Interstitial quartz and granophyre are rare in HZ' and LZa', but increase through LZb', becoming
342 abundant in LZc', MZ' and UZ'. On the grain scale, both quartz and granophyric intergrowths form
343 interstitial bodies typically bounded by the randomly oriented tabular plagioclase grains, and
344 commonly associated with chlorite (Figure 8f): locally, granophyre is so abundant that the euhedral
345 plagioclase grains are entirely surrounded. The quartz component of the granophyre may form thin
346 plates, inverted from primary tridymite due to the low lithostatic pressure (Figure 8d; Lindsley *et al.*,
347 1969). Late-stage hydrothermal alteration is widespread.

348

349 **Evidence of separation of mafic and felsic components in the Layered Series**

350 The upper part of LZc is notable for a series of highly oxide-rich modally-graded layers, ranging in
351 thickness from ~10 cm to ~30 cm (Weatherley *et al.*, 2018). Locally, the sharply-defined base of these
352 layers is underlain by a felsic layer up to 2 cm thick (Figure 9), containing plagioclase of a similar
353 grain size to that in the underlying gabbros, but with finer-grained augite and Fe-Ti oxides (Figure 6b).
354 While the oxide grains in the felsic layer are associated with Type I reactive symplectites, there are no
355 olivine rims separating oxide from adjacent pyroxene, although such rims are present both below and
356 above the layers.

357 Laterally extensive, essentially planar, modally-graded layers are common in UZa and UZb, separated
358 by up to ~20 m of homogeneous gabbro. These layers are generally 10-20 cm thick and grade from a
359 mafic base rich in pyroxene, olivine and Fe-Ti oxides to a top rich in plagioclase. A previously
360 unremarked feature of these modally-graded layers is that although their base is generally sharply
361 defined, their tops are highly irregular (Figures 10a, b, c, d). The extent of the irregularity increases
362 steadily upwards in the stratigraphy, with the felsic parts of the layers in UZb almost completely
363 detached from the underlying layer, to form irregular wisps and blebs (Figures 10c, d).

364 Several reverse modally-graded layers are present in the lower part of UZa (McBirney & Noyes, 1979:
365 Figure 10e), in the region of the intrusion in which the late-stage pegmatites form well-defined sills and
366 dykes (illustrated in Figure 5 of Larsen & Brooks, 1994), indicative of a thin and rigid mush zone. The

367 reverse modally-graded layers extend laterally over ~ 100 m, and have sharply-defined mafic tops and
368 grade downwards over 10-15 cm to more average gabbroic compositions. Locally, small and irregular
369 anorthositic bodies lie immediately above the tops of the layers (Figure 10e). The mafic tops of these
370 layers are dominated by Paragenesis 2 of Nielsen *et al.* (2015) (Figure 4).

371

372 **The autoliths**

373 The gabbroic troctolites (assigned to HZ' and LZa' by Irvine *et al.* (1998)) are dominated by randomly
374 oriented plagioclase grains with irregular grain boundaries characteristic of *in situ* growth to
375 impingement (Holness *et al.*, 2019) (Figure 11a). Plagioclase core compositions are in the range An₇₀
376 – An₅₉ (Table 2). Pyroxene is abundant, comprising interstitial (commonly poikilitic, generally
377 untwinned) augite and inverted pigeonite. Olivine has a wide range of habits and modes: where rare,
378 it forms small rounded grains (Figure 11b, commonly enclosed by pyroxene), or rims separating augite
379 from plagioclase (Figure 11c), but where common, it forms either well-sintered clusters of subhedral
380 grains, or oikocrysts enclosing plagioclase chadacrysts. Representative bulk compositions are
381 provided in Table 3. We found one autolith, hosted in LZc, in which the olivine grains were surrounded
382 by reactive symplectites of orthopyroxene and plagioclase (Figure 11d) – the Type II symplectites of
383 Holness *et al.* (2011), ascribed to reaction between olivine and a Si-rich interstitial liquid. Fe-Ti oxides
384 form anhedral aggregates and oikocrysts that, in some autoliths, are associated with Type I
385 symplectites (Figure 11e). Pockets of interstitial granophyre are rare. Values of Θ_{cpp} in the gabbroic
386 troctolites are in the range 83.5 – 85.5° (Table 2, with full dataset in Supplementary Appendix).

387 The gabbroic anorthosites (assigned to LZb': Irvine *et al.* 1998; representative bulk compositions in
388 Table 3) are coarser-grained than the gabbroic troctolites (see thin section scans in the Supplementary
389 Appendix, and are characterised by euhedral randomly oriented plagioclase (with core compositions
390 in the range An₆₃ – An₅₂: Table 2), with augite forming large, commonly ophitic grains, many of which
391 have simple (100) twins (Figure 11f). Fe-Ti oxides form anhedral interstitial aggregates, rarely
392 surrounded by Type I symplectites. Olivine forms rare small, anhedral and sometimes interstitial,
393 grains. Quartz is interstitial, locally abundant, and commonly in granophyric intergrowths. Granophyric
394 pockets are always bounded by plagioclase, and variously contain green amphibole, chlorite, apatite
395 and brown mica. Values of Θ_{cpp} in the gabbroic anorthosites are in the range 89 – 91° (Table 2,
396 Supplementary Appendix). The UZa-hosted autolith suggested by Irvine *et al.* (1998) to have been
397 only partially solidified on arrival at the floor, shown in Figure 12, is a gabbroic anorthosite. It has well-
398 defined top and side margins: the value of Θ_{cpp} is the same within 1 cm of the top of the autolith margin
399 (sample SK11-B9-10) as it is in the autolith centre (sample SK11-B9-9) (Table 2).

400 The oxide gabbros (assigned to LZc' and MZ') are almost invariably coarse-grained relative to the
401 gabbroic anorthosites (scans of thin sections in the Supplementary Appendix), with primocrysts of Fe-
402 Ti oxides, augite (commonly with simple (100) twins: Figure 11f) and randomly oriented plagioclase
403 with core compositions in the range An₅₂ – An₅₀ (Table 2). Rare grains of olivine are present as

404 inclusions in oxide or augite. Fe-Ti oxides form anhedral aggregates, commonly with extensive
405 marginal interstitial growth, although small grains included in augite or plagioclase are euhedral.
406 Interstitial pockets in plagioclase-rich regions are filled with single grains of quartz (some of which
407 extend in optical continuity through large regions of the thin section) or granophyric intergrowths.
408 Brown mica and amphibole are minor constituents of these quartz-rich interstitial pockets. A
409 representative bulk composition is provided in Table 3. Type I symplectites are common in regions
410 where there is no interstitial quartz or granophyre. The olivine rims between oxides and pyroxene that
411 are a ubiquitous feature of LZc and MZ are only very rarely present, even within ~1 mm of the autolith
412 margin. Values of Θ_{cpp} in the oxide gabbros are in the range 95 – 97° (Table 2, Supplementary
413 Appendix).

414 We examined several samples from an elongate, composite autolith hosted by MZ gabbro. Autolith
415 SK11-B8 (location shown in Figure 1) comprises three layers parallel to the long axis of the
416 outcropping surface, the upper two of which are oxide-rich gabbro, while the base comprises a
417 gabbroic troctolite. The value of Θ_{cpp} in the upper two layers is 95 – 95.5°, with a corresponding
418 plagioclase composition of An₅₁, whereas that in the lower gabbroic troctolite is 85 ± 2° (with
419 plagioclase of An₅₉) (Table 2, Supplementary Appendix).

420

421 **Rims, rinds and segregations associated with the autoliths**

422 *Paired segregations and their relationship with autoliths*

423 Following the assertion by McBirney & Sonnenthal (1990) that the paired mafic and felsic segregations
424 were formed as a consequence of metasomatism, we focussed on the spatial relationships between
425 these features and the autoliths. Examples of paired mafic and felsic segregations in close proximity
426 to autoliths are not common, but where present invariably display the same spatial relationships as
427 those in the host gabbros (e.g. Figure 3). Figure 13a shows an example of a large gabbroic anorthosite
428 autolith in LZb on Uttental Plateau, which is immediately underlain by large irregular bodies which are
429 felsic at the top, with a sharp contact with a lower mafic portion. The mafic material forms a highly
430 irregular network extending some metres below the autolith (c.f. Figure 3), and the felsic portion locally
431 penetrates the autolith on irregular fractures.

432

433 *Rind rock*

434 A sample of the rind rock dykes (JC-107) cutting the gabbroic troctolite autolith shown in Figures 22
435 and 21B of Irvine *et al.* (1998) is fine-grained, with an almost granular microstructure (Figures 14a, b).
436 It is dominated by augite and plagioclase, which is anhedral, randomly oriented and with low aspect
437 ratio. The value of Θ_{cpp} is 105 ± 2° (Supplementary Appendix). Fe-Ti oxides form anhedral grains and

438 patches commonly separated from the adjacent clinopyroxene by rims of olivine associated with
439 reactive symplectites that replace adjacent plagioclase (Figure 14c). The example of rind rock (JC-
440 100) shown in Figure 17a of Irvine *et al.* (1998), associated with an oxide-rich gabbroic autolith found
441 in MZ, contains not only very well-developed reactive symplectites (Figure 14d), but also small and
442 rare interstitial pockets of quartz, surrounded by strongly normally zoned plagioclase.

443 The group of autoliths illustrated in Figure 23 of Irvine *et al.* (1998) is located in LZc (Figure 7), and
444 belongs to the gabbroic anorthosite category of Irvine *et al.* (1998). A sample of rind rock (JC-59,
445 location shown in Figure 7b) is generally fine-grained though with variable grain size. The finest-
446 grained parts, with an almost granular microstructure, contain abundant prismatic ilmenite with a
447 preferred grain alignment (Figure 14e), with minor apatite forming rounded grains enclosed by
448 plagioclase. The coarser-grained parts contain anhedral olivine with abundant rounded inclusions of
449 plagioclase and Fe-Ti oxides (Figure 14f). Again, Θ_{cpp} is $105 \pm 2^\circ$ (Supplementary Appendix).

450

451 *Mafic and felsic rims*

452 Mafic rims, a few mm in thickness and rich in Fe-Ti oxides, occur at the tops of autoliths from LZc
453 upwards (e.g. Figure 12a). We undertook a detailed examination of the autolith population in a ~200
454 m x 200 m area of LZc on Kraemer Ø. The majority of the autoliths are oxide gabbro, and range from
455 ~10 cm to ~20 m on the longest axis. Their apparent shapes on the outcrop surface range from
456 rounded (with an aspect ratio of ~1) to highly elongate parallel to the layering in the host gabbro (Figure
457 13). The rounded autoliths, regardless of their size, do not have mafic rims (Figure 13b). Mafic rims
458 are present on the more elongate autoliths, forming an oxide-rich layer up to 1 cm thick (Figures 13c,
459 d), found only on their top surface. The mafic rims comprise rounded pyroxene grains (generally
460 smaller than those in the autolith and the overlying gabbro), with subordinate anhedral plagioclase,
461 set in an interconnected aggregate of Fe-Ti oxides (Figure 6c). Well-developed polycrystalline olivine
462 rims separate the Fe-Ti oxides from the pyroxene (similar to those shown in Figure 4), and Type I
463 symplectites are common.

464 A previously undocumented feature is that the most tabular autoliths have not only an upper mafic rim,
465 but also have a corresponding felsic rim (generally < 1 cm thick) along their base (Figures 13e, f).
466 These felsic rims are similar to the felsic material underlying the highly oxide-rich layers in the host
467 gabbro (Figure 9), in that they contain fine-grained pyroxene and Fe-Ti oxides, together with coarse-
468 grained plagioclase, the Fe-Ti oxides are associated with Type I symplectites, and no olivine rims
469 separate oxides from adjacent pyroxene (Figure 6d).

470 There is a systematic relationship between the (apparent) autolith shape and the presence/absence
471 of the rims. There is a gradation from autoliths with no rims, through autoliths with an upper mafic rim,
472 to autoliths with a paired upper mafic and lower felsic rim as the (apparent) aspect ratio of the autolith

473 increases (Figure 15). There is no relationship between rim thickness or composition with either size
474 or composition of the autoliths.

475

476 **DISCUSSION**

477 **Compositional evidence used to support the metasomatic hypothesis**

478 McBirney (1989a) provides the average composition of 20 autoliths (no descriptions or localities are
479 provided) and of 13 samples from UBS- β (MZ') "from which most are thought to have been derived"
480 (*ibid.*): these are given in Table 4 together with a further average composition for the autoliths from
481 Sonnenthal & McBirney (1998) (termed anorthositic blocks in their Table 2). The averaged autolith
482 compositions from these two studies are comparable to those of the gabbroic troctolites shown in
483 Table 3: there is no evidence that McBirney (1989a) and Sonnenthal & McBirney (1998) considered
484 autoliths with compositions typical of the oxide-rich gabbros (e.g. Table 3). Their averaged
485 compositions are richer in the components of anorthitic plagioclase and depleted in iron, TiO₂, K₂O
486 and P₂O₅ compared to published averages of MZ' composition (UBS- β) (McBirney, 1989a; Naslund,
487 1984; Salmonsén & Tegner, 2013), and are most similar to the Salmonsén & Tegner (2013) averages
488 of LZa' and LZb'. The CIPW norm of the average autolith compositions given by McBirney (1989a)
489 and Sonnenthal & McBirney (1998) is richer in plagioclase than that of any of the average UBS
490 compositions (Table 4). The average composition of plagioclase cores in the autoliths analysed by
491 McBirney (1989a) is An_{56.2}. According to the position of the subdivision boundary of Salmonsén &
492 Tegner (2013), Namur *et al.* (2014) and Namur & Humphreys (2018), such an average plagioclase
493 composition is consistent with a source in LZb'.

494 The case for the autoliths having been metasomatized appears to rest entirely on the assumption that
495 they were derived from MZ', perhaps on the basis that much of MZ' is absent from the current
496 exposure. However, the average bulk compositions and plagioclase core compositions presented by
497 the McBirney studies are consistent with a source in LZb'.

498

499 **Where *did* the autoliths come from?**

500 Importantly, the preserved exposure of UBS is limited. Irvine *et al.* (1998) recognised this and
501 suggested that some of the more anorthositic autoliths may have been sourced from a now-eroded
502 part of the roof. That many autoliths were derived from a different part of the roof than that now
503 remaining (and hence that the large missing section of MZ' cannot be used as evidence that they were
504 predominantly derived from MZ') is incontrovertibly demonstrated by the presence of xenoliths of the
505 basaltic country rock in upper MZ on Kraemer Ø, requiring the complete removal of the UBS from a

506 now-eroded region of the roof (Figure 5c; Irvine *et al.*, 1998). The remaining part of the UBS is clearly
507 not representative of the whole.

508 The corollary of this evidence of localised excavation of the entire thickness of the contemporaneous
509 UBS is that LZ' must have been the source of at least some of the autoliths in the Layered Series (in
510 agreement with Wager & Brown (1968) and Irvine *et al.* (1998)). Both average bulk compositions and
511 plagioclase composition in the previously published studies are consistent with those autoliths being
512 sourced from LZb'. The plagioclase compositions reported here confirm the assignment of the three
513 lithologies of Irvine *et al.* (1998) to HZ'/LZa, LZb' and LZc'/MZ', supported by the close correspondence
514 of Θ_{cpp} between the autoliths and UBS.

515

516 **Evidence for recrystallisation: primary vs secondary microstructures**

517 In agreement with Irvine *et al.* (1998), we argue that the wholesale crystallisation advocated by
518 McBirney & Hunter (1995) cannot have taken place and that the autoliths retain not only their original
519 composition but also their original microstructures. Further evidence for retention of their original
520 microstructures is provided by the observation that most have sharply-defined margins on the grain-
521 scale (Irvine *et al.*, 1998; Figure 6a). This sharply-defined margin is manifest also by the absence of
522 olivine rims separating Fe-Ti oxide from pyroxene in the oxide-rich gabbroic autoliths hosted in LZc
523 and MZ, with the change occurring over length-scales commensurate with the grainsize, together with
524 the different values of Θ_{cpp} maintained within a few mm of the margin (observed for the top of autolith
525 SK11-B9: Table 2). These sharply-defined margins demonstrate that the autoliths were generally
526 entirely solid on arrival at the floor (exceptions to this include SK11-B9, Figure 12). Importantly,
527 wholesale metasomatism necessitates the blocks to be melt-bearing, to permit significant mass
528 transport through autoliths many 10's of metres in size (Sonnenthal & McBirney, 1998). Therefore,
529 were the autoliths metasomatized, not only would we need to invoke re-melting, but the Θ_{cpp} of the
530 autolith would be indistinguishable from that of its host since the cooling rate during the last stages of
531 solidification of a metasomatized autolith would be the same as that of the host gabbro.

532 A further argument against the metasomatism hypothesis is that the mafic rinds, argued by McBirney
533 to represent the mafic material removed from the autoliths, are not ubiquitous. The rind rock of Irvine
534 *et al.* (1998) is only present on a small number of autoliths, and even where present, does not fully
535 surround them. Furthermore, the truncation at autolith margins of dykes formed by rind rock (Irvine *et al.*
536 *et al.*, 1998) is inconsistent with a metasomatic origin. The thin mafic rinds are not ubiquitous either and,
537 where present, are confined to autolith top surfaces. Were they a result of metasomatism, they would
538 be more prevalent, with their size and distribution correlating with autolith composition rather than
539 autolith shape.

540

541 **Rind rock: magma chilled entering fractures in the UBS**

542 The fine grain size of the rind rock is consistent with the high nucleation rates expected for rapid chilling
543 and crystallisation due to magma encountering a relatively cold environment. Importantly, the rarity of
544 autoliths associated with rind rock demonstrates the unusual conditions required to form it. The rapid
545 chilling cannot have been due to the quenching of bulk magma around a cold, sinking, fragment broken
546 away from the UBS, since such an origin would result in most autoliths having a complete rind.
547 Furthermore, it would be difficult to account for the rind rock dykes by such a mechanism. We therefore
548 agree with Irvine *et al.* (1998), that it formed by the injection of bulk magma into opening fractures in
549 the UBS, most likely created during ongoing seismic activity, the most vigorous episodes of which
550 were responsible for the concentration of the autoliths in certain stratigraphic horizons (and localised
551 collapse of the MBS: Holness *et al.*, 2022). The presence of rind rock on the surface of some autoliths
552 would then be because the filled and solidified fractures represented a mechanical heterogeneity
553 which became the site for some of the subsequent fractures resulting in complete detachment of
554 material from the UBS.

555 The almost granular microstructure of the rind rock, with Θ_{cpp} close to the expected equilibrium value,
556 is very different to that found in dolerites and is indicative of significant subsolidus textural modification.
557 A similar microstructure is found in other examples of chilled magma in large plutons, such as the
558 base of layers formed in the Kap Edvard Holm intrusion formed by successive batches of incoming
559 magma that flowed along the existing chamber floor (Holness *et al.*, 2012b). The chilled margin of the
560 Skaergaard intrusion itself provides another example of a well-developed granular microstructure. The
561 close approach to subsolidus textural equilibrium in the Skaergaard chilled margin was likely due to
562 its early crystallisation and extended time at high temperatures, whereas the more limited subsolidus
563 equilibration of the rind rock is most likely due to a relatively high temperature at which the UBS
564 fractured, with slow subsolidus cooling caused by most of the heat from the intrusion passing through
565 the roof. That high values of Θ_{cpp} are not seen in either the UBS or the autoliths is both because a fine
566 grain size, and consequent short diffusion distances, together with a low initial value of Θ_{cpp} , and hence
567 large departure from equilibrium, are critical for significant subsolidus textural modification (Holness
568 *et al.*, 2012b).

569

570 **Rims form by differential migration of immiscible liquids in the floor cumulates**

571 In contrast to the rarity of rind rock, the mafic/felsic rims are widely developed around autoliths in LZc
572 and MZ (allowing for constraints due to autolith shape: Figure 15). Given the possibility of variations
573 in the events preceding the arrival of the autoliths at the floor, these rims must have formed after they
574 arrived. Building on our new observations and following Holness *et al.* (2011) and Nielsen *et al.* (2015),
575 we suggest that they are a consequence of differential migration of immiscible liquids in the crystal
576 mush on the floor.

577 Outcrop-scale evidence for differential migration within the floor mush is provided by the felsic material
578 at the base of modally-graded layers (Figure 9), and the wispy tops of modally-graded layers (Figure

579 10), both of which we argue are formed by the upwards-flow of the buoyant silica-rich conjugate. This
580 liquid gets trapped under the Fe-rich base of the overlying material (Figure 9) since the permeability
581 of the mush is not only a function of the interconnectivity of the porosity, but also of the minerals
582 making up the mush. Capillary forces due to the non-wetting nature of Si-rich liquid against the
583 predominantly mafic minerals at the base of the overlying modally-graded layer (Honour *et al.*, 2019;
584 Vukmanovic *et al.*, 2018) would prevent further rise. In contrast, there is nothing preventing the
585 upwards rise of felsic liquid from the modally graded layers shown in Figure 10 into the overlying,
586 relatively plagioclase-rich, later-accumulating mush. We suggest the increasing separation of the felsic
587 material with increasing stratigraphic height (compare Figure 10a with Figures 10c and d) is a
588 consequence of greater mobility of this separating Si-rich conjugate as it forms an larger component
589 of the progressively more fractionated interstitial liquid.

590 We suggest that the reverse modally-graded layers (Figure 10e), with their microstructure
591 characteristic of bodies of Fe-rich liquid (Figure 4; Nielsen *et al.*, 2015), are solidified bodies of Fe-rich
592 liquid which ponded on the top of the thin mush on the chamber floor: the low permeability of the mush
593 and the abundance of plagioclase (against which Fe-rich liquid is non-wetting) prevented the liquid
594 percolating downwards more than a few cm. Upwards-percolation of Si-rich liquid, exsolved from the
595 solidifying ponded Fe-rich liquid, into subsequently deposited crystal mush accounts for the wispy and
596 irregular felsic patches overlying the reverse modally-graded layer (Figure 10e).

597 We further suggest that the example of paired segregations associated with autoliths shown in Figure
598 13a, is evidence for ponding of migrating late-stage interstitial liquid against impermeable fully
599 solidified material, instead of a result of metasomatism. Such paired segregations formed by the
600 unmixing of the ponded liquid, with the dense Fe-rich conjugate sinking to the base, while the buoyant
601 Si-rich liquid rose to the top, locally penetrating the autolith along fractures (Figure 13a).

602 Building on the abundant evidence of migration of unmixed immiscible conjugates in the mush, and
603 the similarity in microstructure and composition of the mafic and felsic rims associated with the
604 autoliths with their compositional counterparts forming the paired late-stage segregations throughout
605 the Layered Series (e.g. Figure 3), we suggest that the thin mafic and felsic rims in LZc and MZ (Figure
606 13) are a consequence of ponding of these two liquids against the impermeable autoliths (c.f.
607 Cawthorn & Street, 1994). Accordingly, the mafic rim forms by the solidification of downwards-
608 percolating Fe-rich liquid, whereas the felsic rim forms from the upwards-percolating Si-rich conjugate.
609 The shape of the autoliths affects the extent to which either kind of rim forms because of limited
610 sideways flow of the interstitial liquid: the more laterally extensive the autolith, the more of a barrier it
611 creates. That felsic bodies are found below only the most tabular autoliths is unlikely to be a
612 consequence of a greater lateral mobility of the relatively inviscid fluid. It is more likely because of its
613 lower abundance in the LZc mush, so it can only accumulate in visible amounts against the most
614 tabular autoliths.

615

616 **THE AUTOLITHS AS A RECORD OF ROOF MUSH EVOLUTION**

617 The confirmation that lithology, plagioclase composition and Θ_{cpp} can be used to identify the source of
618 the autoliths enables a greater understanding of the evolution of the UBS. Firstly, the composite
619 autolith we examined (SK11-B8, Table 2; B8, Figure 1), comprising an upper layer of LZc' material
620 and an underlying LZa' component, can now be understood as representing an unconformity
621 developed within the UBS due to fragmentation. We suggest this autolith is actually upside-down, with
622 the missing LZb' material removed during contemporaneous stoping, resulting in the juxtaposition of
623 later-formed LZc' material on the more primitive LZa' material. A further stoping event during MZ times
624 dislodged the entire autolith, which rotated while it sank and arrived on the floor upside-down.

625 We can also comment on the likely range of mush thickness in the roof zone during late MZ times, on
626 the basis of the morphology of autolith SK11-B9 (LZb'). The irregular morphology at its base points to
627 this autolith having been incompletely solidified at the moment it was dislodged from the roof. That the
628 top had solidified sufficiently to lock in the primary value of Θ_{cpp} , indicates that the mush was only a
629 few tens of metres thick, most likely due to re-melting of this outer part of the UBS immediately prior
630 to dislodging. Conversely, the relatively anorthitic composition of the plagioclase in autoliths JC-2 and
631 JC-12 (Table 2) is consistent with significant mush thickness during LZa and LZb times in their source
632 region. While the value of Θ_{cpp} in these two autoliths is the same as that seen in LZb', the anorthitic
633 plagioclase and interstitial untwinned augite are consistent with an origin in LZa'. This apparent
634 contradiction can be resolved if these two autoliths came from close to the LZa'/LZb' boundary, in a
635 region of thick mush with a significant distance between the step-wise change in Θ_{cpp} (denoting the
636 horizon where solidification was essentially complete) and the arrival of augite on the liquidus of the
637 bulk magma (the magma-mush interface) (Holness *et al.*, 2017a).

638

639 **The thermal history of the UBS**

640 In the absence of subsolidus textural equilibration, Θ_{cpp} provides an indication of super-solidus cooling
641 rate for dolerites and gabbros. The similarity of Θ_{cpp} in the UBS (both *in situ* and autoliths) and
642 previously reported values for the MBS (Holness *et al.*, 2022) is consistent with broadly similar cooling
643 rates. In detail, Θ_{cpp} in the HZ and LZa equivalents of MBS near the roof on the Skaergaard Peninsula
644 is in the range 81-84°, slightly lower than that found for LZa* at Udløberen (Table 1). Values of Θ_{cpp} in
645 the MBS LZb equivalent on the Skaergaard Peninsula are in the range 85-87°, again slightly lower
646 than in LZb* on Udløberen. LZc rocks are generally absent in MBS (Holness *et al.*, 2022), but Θ_{cpp} in
647 the MZ equivalent are in the range 91-92° in the MBS on the Skaergaard Peninsula. The consistently
648 slightly higher values of Θ_{cpp} in UBS, and in the topmost eastern part of the MBS, relative to those on
649 the western wall on the Skaergaard Peninsula, are consistent with a more rapid cooling rate for the
650 top part of the western wall. The country rock in all locations is the overlying plateau lavas, so the
651 difference is most likely linked to the details of the geometry of the intrusion upper contacts.

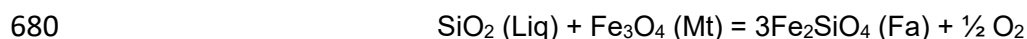
652

653 Evidence of differential migration of immiscible liquids in the UBS

654 The autoliths provide an opportunity to constrain the extent of differential migration of immiscible
655 liquids in the UBS as a whole. While neither the autoliths, nor the remaining exposures of the more
656 evolved parts of LZ' or of MZ', contain the olivine rims separating Fe-Ti oxide from plagioclase and
657 pyroxene primocrysts (Figure 4) that are ubiquitous in their Layered Series equivalents, the autoliths
658 derived from LZb' and LZc'/MZ' contain abundant Type I symplectites, which are very rare in the UBS
659 exposures. A re-examination of the MBS shows that although the olivine rims are present (as stated
660 by Holness *et al.*, 2022), they only occur close to pockets of granophyre. Understanding what these
661 observations may mean in terms of differential migration of immiscible conjugate liquids requires a re-
662 assessment of the processes resulting in the olivine rims.

663 The absence of olivine in MZ was attributed by Wager & Deer (1939) to raised Si activity in the bulk
664 magma, induced by the crystallisation of magnetite (Morse *et al.*, 1980). They therefore accounted for
665 the olivine rims in MZ by arguing that they crystallised from highly evolved interstitial liquid. However,
666 Nwe (1976) showed that the rims have an Mg/Fe ratio similar to any coexisting cumulus olivine and
667 suggested instead that they formed by some unspecified solid-state reaction between iron-rich oxides
668 and pyroxene. McBirney (1996) attributed the rims to reaction between oxides and pyroxene during
669 cooling and equilibration, during which Fe and Mg from the oxides combined with Ca-poor pyroxene
670 exsolved from augite. Similarly, they were suggested to be a result of a progressively reducing oxygen
671 fugacity during late-stage crystallisation by Holness *et al.* (2011), which triggered the reaction
672 magnetite + pyroxene = olivine + Ca + O₂. Nielsen *et al.* (2015) argue that they crystallised from an
673 Fe-rich interstitial liquid rendered out of chemical equilibrium with the surrounding primocrysts due to
674 the loss of an exsolved, buoyant, Si-rich immiscible conjugate.

675 Although Nwe (1976) determined that a relatively high Si activity in the interstitial liquid itself (as
676 required for the reaction suggested by Wager & Deer) could not have been responsible for rim growth,
677 it is possible that overgrowth of magnetite primocrysts from the interstitial liquid creates a boundary
678 layer enriched in SiO₂, which would destabilise magnetite via the FMQ oxygen fugacity buffering
679 reaction:



681 However, this requires only the overgrowth of magnetite from the interstitial liquid, so would be
682 expected wherever there was sufficient interstitial liquid during orthocumulus magnetite growth: it
683 cannot account for the absence of olivine rims in the autoliths, the MBS and UBS, and in LZa and LZb.

684 An alternative explanation takes into account the Nielsen *et al.* (2015) interpretation of Paragenesis 2
685 as a consequence of reaction between plagioclase and pyroxene primocrysts and ponded Fe-rich
686 immiscible melt which had lost appreciable amounts of its Si-rich conjugate, resulting in a decreased
687 silica activity. The parameters likely to play an important role in the formation of the olivine rims are
688 the volume of interstitial melt present when the two-liquid field is reached, the permeability of the mush,

689 and its orientation. Hence, their absence from LZa and LZb is a consequence of the late arrival of the
690 interstitial liquids at the binodal and therefore greater retention of both conjugate liquids within the
691 mush. Their absence from the MBS is because although differential migration of the two liquids could
692 occur, the vertical geometry means that any upwards-migrating Si-rich liquid from any particular level
693 on the wall will be replaced by liquid migrating upwards from lower levels. The situation in the UBS
694 would be complementary to that at the floor, in that any unmixed Fe-rich conjugate would flow
695 downwards, with retention of the Si-rich conjugate. Although this locally resulted in destabilization of
696 magnetite in the UBS and replacement by Fe-rich olivine and pyroxene via reaction with Si-rich liquid
697 (Nielsen *et al.*, 2015), there was no ponding of Fe-rich liquid within the UBS and therefore no
698 dissolution of the earlier-formed primocrysts to create olivine rims.

699 Interestingly, Type I symplectites occur in LZc' autoliths, despite the absence of olivine rims. Clearly,
700 reactive symplectites can form in the absence of significant dissolution of the earlier-formed
701 primocrysts, suggesting either that they form by reaction with Fe-rich liquid at lower temperatures or
702 that a smaller extent of chemical disequilibrium is required. It is notable that there appear to be very
703 few reactive symplectites in the remaining exposures of UBS, with the only examples found near the
704 contact. Given the evidence we have presented earlier that the autoliths retain primary microstructures
705 and compositions, this provides further evidence that the remaining exposure of UBS are not fully
706 representative of the entire roof sequence.

707

708 **CONCLUSIONS**

709 The autoliths preserved in the floor cumulates of the Skaergaard intrusion retain primary
710 microstructures created during solidification at the roof of the intrusion, even within a few millimetres
711 of their margins. The bulk compositions and overall microstructures of the majority of the autoliths are
712 similar to those of the outer parts of the UBS, consistent with a source predominantly within the LZ'
713 subdivision.

714 Importantly, the development of mafic rims previously argued to have formed by metasomatism of the
715 autoliths is strongly associated with autolith shape, rather than composition or size and, on the more
716 tabular autoliths, are paired with an underlying felsic rim. This supports our contention that the UBS
717 autoliths were mainly completely solidified when they arrived at the floor, creating barriers to the
718 outcrop-scale migration of mobile interstitial liquid, resulting in the ponding of interstitial liquid migrating
719 through the mush. This is also consistent with the model of Nielsen *et al.* (2015) accounting for the
720 sulphide-poor PGE-Au mineralization in upper MZ, involving the ponding of dense Fe-rich immiscible
721 melts on the floor, with complementary accumulation of low density components such as plagioclase
722 and immiscible Si-rich melt under the roof. The absence of ponding of significant quantities of Fe-rich
723 liquid in the roof mush zone is supported by the absence of olivine rims separating Fe-Ti oxides from
724 primocrysts of other phases in both the autoliths and the UBS, although the presence of Type I
725 symplectites in the autoliths indicates some reaction due to differential migration in parts of the roof
726 no longer exposed.

727 The Skaergaard autoliths represent a major component of the arguments for microstructures in
728 plutonic rocks being secondary, rather than primary (e.g. McBirney, 2009). While a full assessment of
729 the arguments for the imposition of secondary microstructures on plutonic rocks by wholesale
730 recrystallisation requires re-examination of all other examples used to support this hypothesis, we
731 argue that the Skaergaard autoliths cannot be used in support. Far from having been entirely
732 recrystallised, the Skaergaard autoliths are well-preserved samples of the missing majority of the UBS,
733 offering the only opportunity to establish the true range of composition, microstructural diversity and
734 record of stoping and autolith detachment in this otherwise unavailable part of the intrusion.

735

736 **ACKNOWLEDGEMENTS**

737 We are grateful to Sam Weatherly, Victoria Honour, Gautier Nicoli, Madeleine Humphreys and
738 Brendan Dyck for assistance in the field. Iris Buisman is thanked for the analysis of plagioclase
739 compositions, and we are grateful to Mike Stock for help with re-calculating the results. Gavyn
740 Rollinson helpfully provided QEMSCAN maps to aid the interpretation of several samples. Rune
741 Larsen and Dick Naslund are thanked for helpful and insightful reviews of an earlier version of the
742 manuscript.

743

744 **FUNDING**

745 The collection of many of the autoliths was undertaken by JCØA during graduate work supervised by
746 Neil Irvine, funded by the Carnegie Institution for Science, and under the supervision of Kent Brooks
747 with financial support from the Danish Natural Science Research Council and Carlsberg Foundation.
748 We gratefully acknowledge financial support from Trinity College, Cambridge. This work was also
749 funded by UKRI [grant number NE/N009894/1]. For the purpose of open access, the author has
750 applied a Creative Commons Attribution (CC BY) licence to any Author Accepted Manuscript version
751 arising.

752

753 **DATA AVAILABILITY**

754 All data referred to in this contribution is available either as data tables or in the Supplementary
755 Appendix.

756

757

758

759 **REFERENCES**

- 760 Annen, C., Latypov, R., Chistyakova, S., Cruden, A.R. & Nielsen, T.F.D. (2022) Catastrophic growth
761 of totally molten magma chambers in months to years. *Scientific Advances*, **8**: eabq0394.
- 762 Bartley, J.M., Glazner, A.F. & Coleman, D.S. (2018) Dike intrusion and deformation during growth of
763 the Half Dome pluton, Yosemite National Park, California. *Geosphere*, **14**: 3
- 764 Boudreau, A.E. (2011) The evolution of texture and layering in layered intrusions. *International
765 Geology Review*, **53**: 330-353
- 766 Cawthorn, R.G. & Street, J. (1994) Vertical migration of residual magma in the Upper Zone of the
767 Bushveld Complex. *Mineralogy and Petrology*, **51**: 345-354.
- 768 Fowler, A.C. & Holness, M.B. (2022) The formation of three-grain junctions during solidification. Part
769 II: theory. *Contributions to Mineralogy and Petrology*, **177**: 58. doi.org/10.1007/s00410-022-01921-w
- 770 Glazner, A.F., Bartley, J.M., Coleman, D.S. & Lindgren, K. (2020) Aplite diking and infiltration: a
771 differentiation mechanism restricted to plutonic rocks. *Contributions to Mineralogy and Petrology*, **175**:
772 37. doi.org/ 10.1007/s00410-020-01677-1
- 773 Holness, M.B. (2010) Decoding dihedral angles in melt-bearing and solidified rocks. *Journal of the
774 Virtual Explorer*, **35**: paper 3, doi:10.3809/jvirtex.2010.00265.
- 775 Holness, M.B. (2015) Plagioclase growth rates control three-grain junction geometry in dolerites and
776 gabbros. *Journal of Petrology*, **56**: 2117-2144.
- 777 Holness, M.B., Nielsen, T.F.D. & Tegner, C. (2007) Textural maturity of cumulates: a record of
778 chamber filling, liquidus assemblage, cooling rate and large-scale convection. *Journal of Petrology*,
779 **48**: 141-157.
- 780 Holness, M.B., Anderson, A.T., Martin, V.M., MacLennan, J., Passmore, E. & Schwindinger, K.
781 (2007) Textures in partially solidified crystalline nodules: a window into the pore structure of slowly
782 cooled mafic intrusions. *Journal of Petrology*, **48**: 1243-1264.
- 783 Holness, M.B., Stripp, G., Humphreys, M.C.S., Veksler, I.V., Nielsen, T.F.D. & Tegner, C. (2011)
784 Silicate liquid immiscibility within the crystal mush: late-stage magmatic microstructures in the
785 Skaergaard Intrusion, East Greenland. *Journal of Petrology*, **52**: 175-222.
- 786 Holness, M.B., Richardson, C. & Helz, R.T. (2012a) Disequilibrium dihedral angles in dolerite sills: a
787 new proxy for cooling rate. *Geology*, **40**: 795–798.
- 788 Holness, M.B., Humphreys, M.C.S., Sides, R., Helz, R.T. & Tegner, C. (2012b) Toward an
789 understanding of disequilibrium dihedral angles. *Journal of Geophysical Research*, **117**: B06207.
790 doi: 10.1029/2011JB008902
- 791 Holness, M.B., Namur, O. & Cawthorn, R.G. (2013) Disequilibrium dihedral angles in layered
792 intrusions: a microstructural record of fractionation. *Journal of Petrology*, **54**: 2067-2093.
- 793 Holness, M.B., Tegner, C., Namur, O. & Pilbeam, L. (2015) The earliest history of the Skaergaard
794 magma chamber: a textural and geochemical study of the Cambridge drill core. *Journal of Petrology*,
795 **56**: 1199-1227.
- 796 Holness, M.B., Neufeld, J.A., Gilbert, A.J. & Macdonald, R. (2017b) Orientation of tabular mafic
797 intrusions controls convective vigour and crystallisation style. *Journal of Petrology*, **58**: 2035–2053.
- 798 Holness, M.B., Tegner, C., Nielsen, T.F.D. & Charlier, B. (2017a) The thickness of the mushy layer
799 on the floor of the Skaergaard magma chamber at apatite saturation. *Journal of Petrology*, **58**: 909-
800 932.

- 801 Holness, M.B., Stock, M.J. & Geist, D. (2019) Magma chambers versus mush zones: constraining the
802 architecture of sub-volcanic plumbing systems from microstructural analysis of crystalline enclaves.
803 *Philosophical Transactions of the Royal Society A*, **377**: 20180006.
804 <http://dx.doi.org/10.1098/rsta.2018.0006>
- 805 Holness, M.B., Humphreys, M.C.S., Namur, O., Andersen, J.C. Ø., Tegner, C. & Nielsen, T.F.D. (2022)
806 Crystal mush growth and collapse on a steep wall: the Marginal Border Series of the Skaergaard
807 Intrusion, East Greenland. *Journal of Petrology*, **63**: 1-21.
- 808 Honour, V.C. Holness, M.B., Partidge, J.L. & Charlier, B. (2019) Microstructural evolution of silicate
809 immiscible liquids in ferrobasalts. *Contributions to Mineralogy and Petrology*, **174**: 77.
- 810 Hoover, J.D. (1989) Petrology of the Marginal Border Series of the Skaergaard Intrusion. *Journal of*
811 *Petrology*, **30**: 399–439.
- 812 Humphreys, M.C.S. (2011) Silicate liquid immiscibility within the crystal mush: evidence from Ti in
813 plagioclase from the Skaergaard intrusion. *Journal of Petrology*, **52**: 147-174.
- 814 Irvine, T.N. (1980) Observations on layering in the Skaergaard intrusion. *Carnegie Institution of*
815 *Washington Yearbook*, **79**: 257-262.
- 816 Irvine, T.N. (1987) Layering and related structures in the Duke Island and Skaergaard intrusions:
817 similarities, differences and origins. In: Parsons, I. (ed.) *Origins of Igneous Layering*, pp. 185-245. D.
818 Reidel Publishing Company.
- 819 Irvine, T.N., Andersen, J.C.Ø. & Brooks, C.K. (1998) Included blocks (and blocks within blocks) in the
820 Skaergaard intrusion: geologic relations and the origins of rhythmic modally graded layers. *Geological*
821 *Society of America Bulletin*, **110**: 1398-1447.
- 822 Jakobsen, J.K., Veksler, I.V., Tegner, C. & Brooks, C.K. (2005) Immiscible iron- and silica-rich melts
823 in basalt petrogenesis documented in the Skaergaard intrusion. *Geology*, **33**: 885-888.
- 824 Kays, M.A. & McBirney, A.R. (1982) Origin of the picrite blocks in the Marginal Border Group of the
825 Skaergaard intrusion, East Greenland. *Geochimica et Cosmochimica Acta*, **46**: 23-30.
- 826 Larsen, R.B. & Brooks, C.K. (1994) Origin and evolution of gabbroic pegmatites in the Skaergaard
827 intrusion, East Greenland. *Journal of Petrology*, **35**: 1651-1679.
- 828 Lindsley, D.H., Brown, G.M. & Muir, I.D. (1969) Conditions of ferrowollastonite–ferrohedenbergite
829 inversion in the Skaergaard intrusion, East Greenland. *Mineralogical Society of America Special*
830 *Paper*, **2**: 193–201.
- 831 Maaløe, S. (1976) Zoned plagioclase of the Skaergaard intrusion, East Greenland. *Journal of*
832 *Petrology*, **17**: 398-419.
- 833 Markl, G. (2005) Mullite-corundum-spinel-cordierite-plagioclase xenoliths in the Skaergaard Marginal
834 Border Group: multi-stage interaction between metasediments and basaltic magma. *Contributions to*
835 *Mineralogy and Petrology*, **149**: 196-215.
- 836 McBirney, A.R. (1975) Differentiation of the Skaergaard Intrusion. *Nature*, **253**: 691-694
- 837 McBirney, A.R. (1979) Effects of assimilation, in Yoder, H.S., Jr., ed., *The evolution of the igneous*
838 *rocks, Fiftieth Anniversary Perspectives*: Princeton, New Jersey, Princeton University Press, pp. 307–
839 338.
- 840 McBirney, A.R. (1987) Constitutional zone refining of layered intrusions. In: Parsons, I. (ed.) *Origins*
841 *of Igneous Layering*, pp. 437-452. D. Reidel Publishing Company.
- 842 McBirney, A.R. (1989a) The Skaergaard layered series: I. Structure and average compositions.
843 *Journal of Petrology*, **30**: 363–397.

- 844 McBirney, A.R. (1989b) *Geological map of the Skaergaard Intrusion, East Greenland*. In: Eugene,
845 *Department of Geology*. University of Oregon, p.1:20 000.
- 846 McBirney, A.R. (1995) Mechanisms of differentiation in the Skaergaard Intrusion. *Journal of the*
847 *Geological Society, London*, **152**: 421-435
- 848 McBirney, A.R. (1996) The Skaergaard intrusion, in Cawthorn, R.G. (ed.), *Layered intrusions*
849 (Developments in Petrology 15): Amsterdam, Elsevier, pp. 147–180
- 850 McBirney A.R. (2009) Factors governing the textural development of Skaergaard gabbros: a review.
851 *Lithos*, **111**: 1-5.
- 852 McBirney, A.R. & Hunter, R.H. (1995) The cumulate paradigm reconsidered. *The Journal of Geology*,
853 **103**: 114-122.
- 854 McBirney, A.R. & Nakamura, Y (1974) Immiscibility in late-stage magmas of the Skaergaard intrusion.
855 *Carnegie Institution of Washington Yearbook*, **73**: 348-352.
- 856 McBirney, A.R. & Noyes, R.M. (1979) Crystallisation and layering of the Skaergaard intrusion. *Journal*
857 *of Petrology*, **20**: 487-554.
- 858 McBirney, A.R. & Sonnenthal, E.L. (1990) Metasomatic replacement in the Skaergaard Intrusion, East
859 Greenland: Preliminary observations. *Chemical Geology*, **88**: 245–260.
- 860 Morse, S. A. (2011) The fractional latent heat of crystallising magma. *Ameri-can Mineralogist*, **96**:
861 682–689.
- 862 Morse, S.A., Lindsley, D.H. & Williams, R.J. (1980) Concerning intensive parameters in the
863 Skaergaard intrusion. *American Journal of Science*, **280A**: 159-170.
- 864 Namur, O., Higgins, M.D. & Vander Auwera, J. (2015) The Sept Iles Intrusive Suite, Quebec,
865 Canada. In: Charlier, B., Namur, O., Latypov, R. & Tegner, C. (eds.) *Layered Intrusions*. Springer.
866 Dordrecht, Heidelberg, New York, London. p. 465-516.
- 867 Namur, O. & Humphreys, M.C.S. (2018) Trace element constraints on the differentiation and crystal
868 mush solidification in the Skaergaard Intrusion, Greenland. *Journal of Petrology*, **59**: 387-418.
- 869 Naslund, H.R. (1984a) Petrology of the Upper Border Series of the Skaergaard intrusion, East
870 Greenland: *Journal of Petrology*, **25**: 185–212.
- 871 Naslund, H.R. (1984b) Supersaturation and crystal growth in the roof-zone of the Skaergaard magma
872 chamber. *Contributions to Mineralogy and Petrology*, **86**: 89-93.
- 873 Naslund, H.R. (1986) Disequilibrium partial melting and rheomorphic layer formation in the contact
874 aureole of the Basistoppen sill, East Greenland. *Contributions to Mineralogy and Petrology*, **93**: 359–
875 367.
- 876 Nielsen, T.F.D. (2004). The shape and volume of the Skaergaard Intrusion, East Greenland:
877 Implications for mass balance and bulk composition. *Journal of Petrology*, **45**: 507-530.
- 878 Nielsen, T.F.D., Andersen, J.C.Ø., Holness, M.B., Keiding, J.K., Rudashevsky, N.A., Rudashevsky,
879 V.N., Salmonsén, L.P., Tegner, C. & Veksler, I.V. (2015) The Skaergaard PGE and gold deposit: the
880 result of *in situ* fractionation, sulphide saturation, and magma chamber-scale precious metal
881 redistribution by immiscible Fe-rich melt. *Journal of Petrology*, **56**: 1643-1676.
- 882 Nielsen, T.F.D., Brooks, C.K. & Keiding, J.K. (2019) Bulk liquid for the Skaergaard intrusion and its
883 PGE-Au mineralization: composition, correlation, liquid line of descent, and timing of sulphide
884 saturation and silicate-silicate immiscibility. *Journal of Petrology*, **60**: 1853-1880.
- 885 Nwe, Y.Y. (1976) Electron-probe studies of the earlier pyroxenes and olivines from the Skaergaard
886 Intrusion, East Greenland. *Contributions to Mineralogy and Petrology*, **55**: 105-126.

- 887 Pang, K.N., Li, C., Zhou, M.F. & Ripley, E.M. (2009) Mineral compositional constraints on petrogenesis
888 and oxide ore genesis of the late Permian Panzhihua layered gabbroic intrusion, SW China. *Lithos*,
889 **110**: 199-214.
- 890 Riegger, O.K. & van Vlack, L.H. (1960) Dihedral angle measurements. *Transactions of the*
891 *Metallurgical Society of the AIME*, **218**: 933–935.
- 892 Salmonsén, L.P. & Tegner, C. (2013) Crystallisation sequence of the Upper Border Series of the
893 Skaergaard Intrusion: revised subdivision and implications for chamber-scale magma homogeneity.
894 *Contributions to Mineralogy and Petrology*, **165**: 1155-1171.
- 895 Salmonsén, L.P., Tegner, C., Barfod, G.H. & Leshner, C.E. (2014) Compositional differences between
896 roof and floor rocks of the Skaergaard intrusion. *EGU General Assembly Conference Abstracts*,
897 2014EGUGA..1612525S
- 898 Sonnenthal, E.L. (1992) Geochemistry of dendritic anorthosites and associated pegmatites in the
899 Skaergaard intrusion, East Greenland: evidence for metasomatism by a chlorine-rich fluid. *Journal of*
900 *Volcanology and Geothermal Research*, **52**: 209-230.
- 901 Sonnenthal, E.L. & McBirney, A.R. (1998) The Skaergaard Layered Series. Part IV. Reaction-transport
902 simulations of foundered blocks. *Journal of Petrology*, **39**: 633-661
- 903 Stickels, C.A. & Hücke, E.E. (1964) Measurement of dihedral angles. *Transactions of the Metallurgical*
904 *Society of the AIME*, **230**: 795–801.
- 905 Taylor, H.P. Jr. & Forester, R.W. (1979) An oxygen isotopic study of the Skaergaard Intrusion and its
906 country rocks: a description of a 55-m.y. old fossil hydrothermal system. *Journal of Petrology*, **20**: 355-
907 419.
- 908 Vukmanovic, Z., Holness, M.B., Monks, K. & Andersen, J.C.Ø. (2018) The Skaergaard trough layering:
909 sedimentation in a convecting magma chamber. *Contributions to Mineralogy and Petrology*, **173**: 43.
- 910 Wager, L.R. (1960) The major element variation of the Layered Series of the Skaergaard intrusion and
911 a re-estimation of the average composition of the Hidden Layered Series and of the successive
912 residual magmas. *Journal of Petrology*, **1**: 364-398.
- 913 Wager, L.R. & Deer, W.A. (1939) Geological investigations in East Greenland, Part III. The petrology
914 of the Skaergaard Intrusion, Kangerdlugssuaq, East Greenland. *Meddeleser om Grønland*, **105**.
- 915 Wager, L. R. & Brown, G. M. (1968) *Igneous Rocks*. Edinburgh, Oliver and Boyd, 588 p.
- 916 Weatherley, S., Andersen, J.C.Ø., Holness, M.B., Dyck, B.J., Nicoli, G. & Honour, V.C. (2018)
917 Combined 'sedimentary' and in-situ origin for magmatic Fe-Ti-V deposits: new insights from the
918 Skaergaard intrusion, East Greenland. 33rd Nordic Geological Winter Meeting.
919 [https://2dggf.dk/foreningen/33rd-nordic-geological-winter-meeting/ngwm-2018-abstracts/1-igneous-](https://2dggf.dk/foreningen/33rd-nordic-geological-winter-meeting/ngwm-2018-abstracts/1-igneous-rocks-and-processes/#5)
920 [rocks-and-processes/#5](https://2dggf.dk/foreningen/33rd-nordic-geological-winter-meeting/ngwm-2018-abstracts/1-igneous-rocks-and-processes/#5)
- 921 Wotzlaw, J.-F., Bindeman, I.N., Schaltegger, U., Brooks, C.K. & Naslund, H.R. (2012) High-resolution
922 insights into episodes of crystallization, hydrothermal alteration and remelting in the Skaergaard
923 intrusive complex. *Earth and Planetary Science Letters*, **355–356**: 199–212.
- 924

925 **FIGURE CAPTIONS**

926 Figure 1 – Schematic map of the Skaergaard Intrusion (after McBirney, 1989b). The location of the
927 detailed map of the southern part of the intrusion shown in Figure 2 is outlined by the blue box. The
928 locations of the autoliths analysed as part of this study are also shown (autoliths labelled B are the
929 SK11-B samples listed in Table 2, and SK11-B9 is illustrated in Figure 12).

930 Figure 2 – Detailed map (after McBirney, 1989b) of the southern part of the Skaergaard Intrusion, with
931 the location of the samples examined for this study. The various schemes for subdividing the UBS are
932 also shown, together with the composition of plagioclase cores used to define the boundaries.

933 Figure 3 – Paired felsic and mafic segregations in the Skaergaard Layered Series. (a) Felsic wisp-like
934 segregations forming a network in LZb on Uttental Plateau. Note the corresponding network of mafic
935 wisp-like segregations immediately underlying the felsic network. Handheld GPS for scale. (b)
936 Localised zone rich in late-stage liquid segregations in upper LZc, Kraemer Ø. The felsic segregations
937 overly the associated mafic segregations, and the localised disruption of the fabric in the gabbroic host
938 indicates fluid movement in a deformable mush. (c) A pocket of segregated interstitial liquid containing
939 both felsic and mafic components. The rounded top may be related to the high viscosity of the felsic
940 liquid, in comparison to the irregularity of the lower relatively inviscid mafic conjugate. Upper LZc on
941 Kraemer Ø. (d) Close-up of the right side of the segregation in (c).

942 Figure 4 – photomicrographs of Paragenesis 2, taken under crossed polars. (a) Sample 591633 from
943 LZc, showing the olivine rims separating Fe-Ti oxides (ox) from augite (cpx). Arrows point to examples
944 of Type I symplectites. Scale bar is 500 μm long. (b) The top of the reverse modally-graded layer
945 shown in Figure 12e, displaying olivine rims separating Fe-Ti oxides from recrystallised clinopyroxene.
946 The rims are monocrystalline and in optical continuity with nearby olivine primocrysts (examples are
947 arrowed), but polycrystalline where there are no nearby olivine primocrysts. Scale bar is 1 mm long.

948 Figure 5 – Xenoliths and autoliths in the Skaergaard Layered Series. (a) xenolith of Precambrian
949 gneissic country rock near the contact on Uttental Plateau. (b) Accumulation of xenoliths of ultramafic
950 material near the contact on Uttental Plateau. Rifle for scale. (c) Group of metabasic xenoliths (rusty
951 orange colour) derived from the plateau lavas overlying the intrusion, in MZ in the southern part of
952 Kraemer Ø. The arrows show thin mafic rims. Hammer for scale. (d) Autolith derived from the UBS in
953 LZb on Kraemer Ø. Note the minor deflection of modal layering underneath the autolith indicative of
954 limited and localised compaction. Hammer for scale.

955 Figure 6 – Scans of thin sections, showing contacts between autolith and the host gabbro. The
956 sections are all oriented so the images are the right way up. All scale bars 5 mm long. (a) the lower,
957 sharply defined, contact between autolith SK11-B1 and host gabbro (LZc). The autolith comprises
958 primocrysts of plagioclase and (rare) olivine (some of which extends to form thin rims separating
959 plagioclase and augite: the location of the rim shown in Figure 11c is arrowed), with interstitial augite,
960 whereas the LZc host rock comprises primocrysts of plagioclase, olivine, augite and Fe-Ti oxides.
961 Dihedral angles form clearly distinct populations in autolith and host (Table 2). (b) The felsic layer
962 immediately underlying the oxide-rich mafic base of a modally graded layer in LZc (collected from
963 close to those shown in Figure 9). The approximate position of the base and top of the felsic layer are
964 shown by the dashed red lines. (c) Example of a mafic rind developed at the top of an autolith. The
965 autolith is an oxide-rich gabbro and the host gabbro is LZc. (d) Example of a felsic rind developed at
966 the base of an oxide-rich gabbro autolith hosted by LZc gabbro (typical of those shown in Figures 13e,
967 f). The approximate positions of the base of the autolith and the lower contact of the felsic rind are
968 shown by the red dashed lines. Note the finer grain size of the augite in the felsic rind compared to the
969 host gabbro.

970 Figure 7 – (a) Rind rock surrounding some of a group of blocks in LZc (stated to be MZ by Irvine *et al.*
971 (1998) before the LZc/MZ boundary was re-mapped), viewed looking towards SE. This location is that
972 of Figure 12F of Irvine *et al.* (1998). Hammer for scale. (b) The setting of the blocks shown in (a),
973 re-drawn and simplified from Figure 23 of Irvine *et al.* (1998). Pale grey denotes autoliths, with rind rock
974 shown as dark grey. The lines denote Fe-rich modal layering. The location of rind rock sample JC-59
975 is shown by the circle, and that of Figure (a) is shown by the red box.

976 Figure 8 – photomicrographs of the UBS. Locations of the samples are shown in Figure 2. (a)
977 Randomly oriented plagioclase with irregular grain margins indicative of *in situ* growth to impingement.
978 Olivine (ol) forms clusters of anhedral grains. Sample EG 1724. Scale bar is 1 mm long. (b) Randomly
979 oriented plagioclase with anhedral primocrysts of olivine, together with poikilitic clinopyroxene (cpx)
980 and interstitial Fe-Ti oxides (ox). Sample EG 2274. Scale bar is 1 mm long. (c) UZ' gabbro, with
981 abundant interstitial granophyre (gr), euhedral Fe-Ti oxides, and clusters of anhedral clinopyroxene.
982 Sample EC 49. Scale bar is 1 mm long. (d) The clinopyroxene in other regions of the same sample as
983 (c) is dendritic. The quartz in the granophyre forms plates (elongate when viewed edgewise), indicative
984 of an origin as tridymite. Scale bar is 1 mm long. (e) LZc' gabbro with abundant euhedral grains of Fe-
985 Ti oxides. The interstitial augite forms aggregates of anhedral grains. Sample EC 37. Scale bar is 1
986 mm long. (f) Highly granophyric material from the inner parts of the UBS, with abundant chlorite (chl)
987 in the centres of the granophyric patches, which are sufficiently large to isolate individual euhedral
988 plagioclase grains (pl). Sample EG 1876. Scale bar is 1 mm long.

989 Figure 9 – Modal layering in the upper part of LZc on Kraemer Ø. (a) The well-defined oxide-rich bases
990 of several of the modally-graded layers are immediately underlain by a strongly felsic layer (examples
991 are arrowed). This outcrop also contains a number of autoliths, aligned with their long axes (in 2D
992 cross section) parallel to the layering. Those autoliths marked with an asterisk have no mafic top rims,
993 while that marked with a white circle has a well-defined mafic rim along its top surface. (b) Closer view
994 of the modally-graded layering showing the well-defined felsic layers immediately underlying their
995 oxide-rich base (arrowed).

996 Figure 10 – Modally-graded layers in UZ of the Skaergaard intrusion. (a) In UZa, the isolated modally-
997 graded layers have irregular upper surfaces, with the felsic material forming elongate fingers into the
998 overlying host homogeneous gabbro (an example is arrowed). The pole on the right side of the image
999 is 1 m long. (b, c, d) In UZb, the irregularity of the tops of the modally-graded layers is greater than in
1000 UZa, with increasing extent of detachment of the felsic material from the underlying layer with
1001 stratigraphic height. This detachment is complete in the upper parts of UZb, with the felsic component
1002 forming irregular separate wisps and lenses (d). (e) A reverse modally-graded layer in UZa, near the
1003 layer-parallel pegmatite sills shown in Figure 5 of Larsen & Brooks (1994). Note the felsic regions
1004 (arrowed) immediately overlying the layer. Hammer handle for scale.

1005 Figure 11 – photomicrographs of autoliths (locations shown in Figure 1). (a) JC31, a gabbroic troctolite
1006 containing highly anhedral olivine (ol). The plagioclase grains are randomly oriented, with non-planar
1007 grain boundaries with no orientation relationship with likely growth faces, indicative of substantial *in*
1008 *situ* growth to impingement. Photographed under crossed polars. Scale bar is 1 mm long. (b) JC24A,
1009 a gabbroic troctolite containing subhedral olivine as isolated grains or clusters, together with interstitial
1010 augite. Photographed in plane polarised light. Scale bar is 1 mm long. (c) SK11-B1, a gabbroic
1011 troctolite containing interstitial augite that is locally rimmed with olivine (arrowed). Photographed under
1012 crossed polars. Scale bar is 500 μm long. (d) JC13, a gabbroic troctolite, in which the olivine
1013 primocrysts are locally rimmed with Type I symplectites. Photographed in plane polarised light. Scale
1014 bar is 250 μm long. (e) JC105, an oxide-rich gabbro, with Type I symplectites (examples are arrowed).
1015 Olivine rims separate the oxide from augite, with a rare example of an anhedral olivine grain enclosed
1016 by the augite. Photographed under crossed polars. Scale bar is 1 mm long. (f) JC23, an oxide-rich

1017 gabbro, showing the (100) simple twins in augite primocrysts. Photographed under crossed polars.
1018 Scale bar is 1 mm long.

1019 Figure 12 – Autolith SK11-B9 (location, B9, shown in Figure 1). (a) viewed looking SE, with the top of
1020 the autolith at the left, and the northern side running along the base of the image. Note the sharply
1021 defined and straight side of the autolith. The location of sample SK11-B9-10 is shown by the asterisk.
1022 Note the thin Fe-rich margin along the top of the autolith (arrowed). (b) the northern side of the autolith,
1023 viewed looking east, up the stratigraphy. The base is highly irregular and lobate, with patchy felsic
1024 margins.

1025 Figure 13 – (a) Large relatively felsic autolith in LZb (the width in this field of view is ~10m) underlain
1026 by a group of irregular bodies of segregated late-stage liquid, separated into an upper, volumetrically
1027 dominant, felsic portion (asterisks) and a lower mafic portion (white arrows pointing up). The gabbro
1028 underlying these contains an irregular network of mafic segregations (white arrows pointing down).
1029 The felsic part of the segregation fills an irregular fracture in the autolith (black arrows). The remainder
1030 of the autoliths shown here are from LZc on Kraemer Ø. (b) A pair of rounded autoliths (the smaller of
1031 the pair is marked with an asterisk) with no compositional variations at their margins. (c) An elongate
1032 autolith (lower part of image) has a well-defined mafic rim on its top surface, whereas smaller, more
1033 rounded, autoliths (two are marked by arrows and the third by an asterisk) have no compositional
1034 changes at their margins. (d) An elongate autolith with a well-defined mafic rim on the top contact, and
1035 a poorly-defined felsic rim locally developed (immediately above the scale bar). The asterisk shows a
1036 rounded autolith with no rim. (e) A group of autoliths comprising a trio of highly elongate autoliths with
1037 both mafic and felsic rims (the felsic rims are arrowed). The autolith marked with an asterisk has no
1038 rims. (f) A highly elongate autolith with well-developed paired mafic and felsic rims. The felsic rim at
1039 the base is arrowed. This image shows only a portion of the autolith, which extends a further metre to
1040 the right.

1041 Figure 14 – Photomicrographs of rind rock. (a), (b) and (c) Rind rock forming dykes cutting the autolith
1042 illustrated in Figures 22 and 21B of Irvine *et al.* (1998) under crossed polars (a) and in plane polarised
1043 light (b). Note the close approach to a granular microstructure and absence of a grain preferred
1044 orientation for the plagioclase. Oxides are either ilmenite (elongate) or magnetite (anhedral). (c) shows
1045 olivine rims separating magnetite from clinopyroxene, and some small and very fine-grained reactive
1046 symplectites (arrowed). Scale bar is 1 mm long in (a) and (b), and 250 μm long in (c). (d) Well-
1047 developed reactive symplectites and olivine rims associated with anhedral aggregates of Fe-Ti oxides
1048 in rind rock associated with an LZc' autolith in MZ, illustrated in Figure 17a of Irvine *et al.* (1998). Plane
1049 polarised light. Scale bar is 500 μm long. (e) Rind rock associated with an autolith in LZc and illustrated
1050 in Figure 23 of Irvine *et al.* (1998), displaying a preferred orientation of elongate ilmenite grains. Plane
1051 polarised light, Scale bar is 500 μm long. (f) Same sample as (e), showing olivine oikocrysts with
1052 inclusions of plagioclase and Fe-Ti oxides in the more coarse-grained part. Plane polarised light. Scale
1053 bar is 1 mm long.

1054 Figure 15 – The apparent aspect ratio of 88 autoliths in LZc on Kraemer Ø, measured on outcrop
1055 surfaces approximately perpendicular to the layering, divided according to whether the autoliths show
1056 no rims, mafic rims only (on their top surfaces), or paired mafic and felsic rims.